The Astrophysical Journal, 908:35 (15pp), 2021 February 10 https://doi.org/10.3847/1538-4357/abd4e8

Dependence of the IBEX Ribbon Geometry on Pitch-Angle Scattering outside the Heliopause

E. J. Zirnstein[1], M. A. Dayeh[2,3], and J. Heerikhuisen[4,5]
[1] Department of Astrophysical Sciences, Princeton University, Princeton, NJ 08544, USA; ejz@princeton.edu
[2] Southwest Research Institute, San Antonio, TX 78228, USA
[3] Department of Physics and Astronomy, University of Texas at San Antonio, San Antonio, TX 78249, USA
[4] Department of Mathematics and Statistics, University of Waikato, Hamilton, New Zealand
[5] Department of Space Science, University of Alabama in Huntsville, Huntsville, AL 35899, USA
Received 2020 May 1; revised 2020 November 23; accepted 2020 December 16; published 2021 February 10

Abstract

Interstellar Boundary Explorer (IBEX) observations of the "ribbon" of enhanced energetic neutral atom (ENA) fluxes show that it is a persistent feature that approximately forms a circle in the sky, likely formed from secondary ENAs whose source lies outside the heliopause. The IBEX ribbon's geometry (radius and center) depends on ENA energy and is believed to be influenced by the draping of the ISMF and the latitudinal structure of the SW. In this study, we demonstrate that the ribbon's geometry also depends on the pitch-angle scattering rate of ions outside the heliopause, which we simulate under strong and weak-scattering limits. The ribbon radius in the weak-scattering model is ∼4° larger than IBEX observations at most energies, and the strong-scattering model produces radii statistically consistent with IBEX at 1.1–2.7 keV. The simulated ribbon center is shifted between ∼2° and 5° along the *B*–*V* plane away from the IBEX center for the weak and strong limits, respectively, suggesting that the pristine ISMF far from the heliosphere is shifted ∼2°–5° away from our simulated ISMF toward the VLISM inflow direction. However, the magnitude needs to be decreased from ∼3 to 2 μG for the weak-scattering model to be consistent with the IBEX ribbon radius, which seems unlikely. We also find that the presence of interstellar He does not significantly affect the ribbon in the strong-scattering limit but yields weaker agreement with data in the weak limit. Our results slightly favor the strong-scattering limit for the ribbon's origin.

Unified Astronomy Thesaurus concepts: Heliosphere (711); Solar wind (1873); Pickup ions (1239); Interstellar medium (847); Heliosheath (710); Interstellar magnetic fields (845)

1. Introduction

The solar wind (SW) plasma emanating from the Sun interacts with the partially ionized, very local interstellar medium (VLISM) forming the heliosphere surrounding our solar system (e.g., Parker 1961; Zank 1999, 2015). The SW travels radially outward from the Sun until it encounters a termination shock (TS) where it is slowed, compressed, and heated. Pickup ions (PUIs) are generated in the heliosphere by photoionization or charge exchange of interstellar neutrals that propagate into the heliosphere from the VLISM. As a non-equilibrated population, PUIs are advected with the SW past the TS, forming a suprathermal ion population in the inner heliosheath (IHS). The SW and interstellar plasmas are separated at the heliosphere's boundary, a tangential discontinuity called the heliopause. Throughout the SW-VLISM interaction, the charge exchange between PUIs and interstellar neutral atoms creates energetic neutral atoms (ENAs) that travel ballistically at ∼keV or greater energies. Some ENAs travel toward Earth and can be detected, while others travel outside the heliosphere and charge exchange in the relatively dense outer heliosheath (OHS) where they form a new PUI population.

The Interstellar Boundary Explorer (IBEX; McComas et al. 2009a) is an Earth-orbiting spacecraft with single-pixel cameras (IBEX-Lo and IBEX-Hi) that creates all-sky maps of neutral atoms traveling toward Earth. These are either interstellar neutral atoms propagating into the heliosphere (e.g., McComas et al. 2009b; Möbius et al. 2009; Bzowski et al. 2019 and references therein) or ENAs produced by charge exchange in the IHS or OHS (e.g., McComas et al. 2009b, 2017, 2018b; Schwadron et al. 2018 and references therein). IBEX-Hi measures ENAs from ∼0.5 to 6 keV from all directions in the sky. It is at these energies that IBEX observations inform us of the suprathermal plasma properties of the outer heliosphere (e.g., Schwadron et al. 2014b; Zirnstein et al. 2017) and the heliosphere's structure (e.g., Reisenfeld et al. 2019; Zirnstein et al. 2018b).

ENAs produced in the IHS that directly propagate back toward Earth primarily form the "globally distributed flux" (GDF) observed by IBEX, with broad enhancements toward the nose and tail of the heliosphere (e.g., McComas et al. 2009b; Schwadron et al. 2014b). Another feature that IBEX observes is the so-called "ribbon" of enhanced ENA fluxes that forms a nearly circular, narrow band across much of the sky (e.g., McComas et al. 2009b, 2017). It is widely believed that the ribbon is formed from the secondary ENA mechanism (e.g., Heerikhuisen et al. 2010). In this mechanism, neutral SW ions propagating radially outward from the Sun are able to travel outside the heliopause before experiencing a high probability of charge exchange in the dense OHS. Charge exchange of neutral SW ions in the OHS creates "pickup ions from neutral solar wind" (PINS) that gyrate around the local interstellar magnetic field (ISMF) draped around the heliosphere. A subsequent charge exchange after a typical time of a few years (for ∼1 keV protons) creates secondary ENAs that may then travel back into the heliosphere and be detected by IBEX, preferentially from directions nearly perpendicular to the ISMF. Note that it is not only neutral supersonic SW ions, but also any neutralized energetic IHS ions that can travel outside the heliopause and become secondary ENAs. The neutral SW dominates the ∼1–3 keV signal observed by IBEX but neutral PUIs and IHS ions are important at lower and higher energies (e.g., Zirnstein et al. 2016a; Schwadron & McComas 2019).

The geometric properties of the IBEX ribbon have been studied in detail. The ribbon's average angular radius and geometric center projected in the sky have been derived as a

function of energy and time (Funsten et al. 2009b, 2013; Dayeh et al. 2019). Dayeh et al. (2019) analyzed the first 9 yr of IBEX observations and found that the ribbon's angular radius is $74.^{\circ}81 \pm 0.^{\circ}65$ and its center in ecliptic J2000 coordinates is $(218.^{\circ}33 \pm 0.^{\circ}68, 40.^{\circ}38 \pm 0.^{\circ}88)$, both averaged over energy and time. Similar to the results of Funsten et al. (2013); Dayeh et al. (2019) found that the ribbon's center has a persistent trend with energy, where the center location at energies <2 keV is spread out close to the *B*–*V* plane (*B* for ISMF, *V* for VLISM inflow direction) and the center location at energies >2 keV lie close to the solar meridional plane. The reason for the trend at low energies is believed to be related to the draping of the ISMF around the heliopause (Zirnstein et al. 2016a) and the trend at higher energies is due to the latitudinal structure of the SW (Swaczyna et al. 2016). There is only a slight dependence of the angular radius of the ribbon on energy, and little variation over time. Thus, at least for the first 9 yr of IBEX observations, the ribbon has unique geometry as a function of energy but remains nearly constant over time.

Recent modeling efforts have shown that the geometric properties of the ribbon may also depend on the pitch-angle scattering rate of PINS outside the heliopause. Zirnstein et al. (2018a, 2019a) simulated the ribbon under the limits of weak (i.e., scatter-free) and strong (i.e., quick isotropization) pitch-angle scattering and compared the simulated ribbon's spectral properties in both cases (see also Chalov et al. 2010; Schwadron & McComas 2013). Zirnstein et al. (2019b) also showed that the ribbon peak appears to be farther from the ISMF direction in the weak compared to the strong-scattering case, suggesting either that the ribbon radius is larger, or the center is offset, in one case compared to the other. This behavior has important implications on our understanding of the source of the IBEX ribbon and the properties of the ISMF, since the pristine ISMF magnitude and direction appear to be inextricably linked to the ribbon's geometry (e.g., Zirnstein et al. 2016b and references therein).

In this study, we present an analysis of IBEX ENA observations of the ribbon in the context of simulations. We simulate the ribbon under weak and strong pitch-angle scattering limits as published previously by Zirnstein et al. (2018a, 2019a) and derive the ribbon's geometric properties under these two limits. In Section 2, we describe the models of the heliosphere and ribbon. In Section 3, we present our simulation results and compare the results between different scattering limits. Finally, in Section 4, we summarize our results and discuss the implications in the context of the ribbon's source and the properties of the pristine ISMF far from the influence of the heliosphere.

2. Model

We follow the methodology from Zirnstein et al. (2018a, 2019a, 2019b) to simulate the heliosphere, neutral SW source, and the ribbon under two opposing limits of pitch-angle scattering. In Sections 2.1–2.3, we briefly summarize the methodology of our simulation.

2.1. Simulation of the Heliosphere

We simulate the ribbon using results from a three-dimensional magnetohydrodynamic (MHD; for plasma) and kinetic (for neutrals) simulation of the SW-VLISM interaction. The heliosphere simulation solves the ideal MHD equations for the plasma and the Boltzmann transport equation for kinetic neutral hydrogen atoms. The plasma and neutral atoms are coupled together by source terms in the MHD mass, momentum, and energy equations via energy-dependent charge exchange and photoionization (e.g., Pogorelov et al. 2008; Heerikhuisen et al. 2009).

2.1.1. Simulation Boundary Conditions

The SW boundary conditions at 1 au from the Sun are the same as those used in our previous work (e.g., Zirnstein et al. 2018a, 2019a, 2019b). Specifically, we set the 1 au values of the plasma density as 5.74 cm^{-3}, temperature as 51,100 K, flow speed as 450 $\mathrm{km\,s}^{-1}$, and magnetic field radial component as 37.5 μG, simulated as a Parker spiral. While the neutral atoms are simulated self-consistently, the grid size in which the neutral atom statistics are accumulated is significantly larger than the angular width of the realistic neutral SW distribution, which prevents us using this grid to correctly model the neutral SW outside the heliopause (see also Florinski & Heerikhuisen 2017). Therefore, similar to our previous work (e.g., Zirnstein et al. 2019b) we model the neutralized SW distribution analytically, following Swaczyna et al. (2016). The neutral SW distribution is propagated beyond the heliopause and is used to generate PUIs (i.e., PINS), and consequently secondary ENAs, in our post-processing model of the ribbon (see Section 2.2).

The VLISM boundary conditions at 1000 au from the Sun are also the same as in our previous work. We set the ISMF magnitude as 2.93 μG with direction $(227.^{\circ}28, 34.^{\circ}62)$ in ecliptic J2000 coordinates (Zirnstein et al. 2016b), the interstellar plasma and neutral temperature and flow speed are 7500 K and 25.4 $\mathrm{km\,s}^{-1}$, respectively. The VLISM inflow direction is $(255.^{\circ}7, 5.^{\circ}1)$ in ecliptic J2000 coordinates (McComas et al. 2015). The interstellar plasma and neutral H densities are set as 0.09 cm^{-3} and 0.154 cm^{-3}, respectively. This allows us to approximately reproduce the distances to the heliopause observed by the Voyager spacecraft (e.g., Gurnett et al. 2013; Stone et al. 2013, 2019) and the filtration of neutral H atoms through the heliosheath, yielding a neutral H density of ~0.09 cm^{-3} at the upwind TS (Bzowski et al. 2009).

We note that a recent analysis of New Horizons' Solar Wind Around Pluto (SWAP; McComas et al. 2008a) observations of interstellar H^{+} PUIs by Swaczyna et al. (2020) found that the interstellar neutral H density at the upwind TS is ~40% larger than previously thought (0.13 cm^{-3} instead of 0.09 cm^{-3}). The immediate implications of this higher density with respect to our analysis suggests that our simulated neutral SW distribution (Section 2.2) will be higher by ~40%. Implementing this higher density requires a more thorough analysis to properly account for the filtration of H through the heliosphere. However, we have analyzed the sensitivity of our results to the interstellar neutral H density by using different neutral H densities heuristically in Equation (1) in Section 2.2 and find that our results for the geometry of the ribbon are not significantly affected by the assumption for the neutral H density.

2.1.2. Simulation Heliospheric Boundaries

The results from our MHD/kinetic simulation are used to compute the ribbon flux. In particular, the MHD plasma, neutral, and magnetic field properties are interpolated from the three-dimensional spherical grid of the simulation solution in order to compute the ENA production rate at all positions outside the simulated heliopause. We note that currently no global model of the heliosphere is able to reproduce the thickness of the IHS as inferred from the Voyager spacecraft

crossings of the TS and heliopause boundaries. Because of this, we are only able to constrain our simulation to reproduce either the TS distance (average of Voyager 1 and 2 distances is ∼89 au) or average heliopause distance (average of Voyager 1 and 2 distances is ∼120 au). Since we are mainly concerned with the production of ribbon ENAs outside the heliopause, where the draping of the ISMF greatly influences the ribbon source (e.g., Zirnstein et al. 2015a), our simulation is constrained to reproduce the heliopause distance of ∼120 au in the Voyager *1* and *2* directions (Gurnett et al. 2013; Stone et al. 2019). Our MHD simulation is solved on a spherical grid, with angular resolution of 1°.5 in latitude and 3° in longitude. The radial grid size Δr increases with distance from the Sun, where $\Delta r = 1.0$ au at 89 au from the Sun, $\Delta r = 1.3$ au at 120 au from the Sun, and $\Delta r = 2.7$ au at 300 au from the Sun.

Our choice of SW boundary conditions for the MHD simulation are a simplified representation of solar maximum-like conditions (i.e., uniform slow SW). In reality, time-dependent SW conditions causes the heliopause to move inward and outward over time, primarily due to changes in SW dynamic pressure. The primary motivation to use latitude-independent SW conditions for our MHD simulation in the current study is so that we use similar MHD simulation assumptions as Zirnstein et al. (2016b), who derived the ISMF based on the IBEX ribbon geometry, to make our current analysis comparable. Changes in SW conditions over time affect the TS distance more than the heliopause, which is plainly seen in previous time-dependent simulation analyses (e.g., Izmodenov et al. 2005). Moreover, if the SW dynamic pressure is approximately latitude independent as shown by *Ulysses* in-situ observations (e.g., McComas et al. 2008b), the distance to the heliopause does not vary strongly with latitude (besides asymmetries induced by the asymmetric SW-VLISM interaction itself, i.e., the tilted ISMF). Therefore, time dependence of the SW, rather than latitudinal asymmetry at a single instant in time, is more effective at moving the heliopause. Unfortunately, we are not yet equipped to model the ribbon geometry as a function of time, therefore we believe using latitude-independent SW conditions is satisfactory to reproduce the distance to the heliopause. We note that some studies use observations from SOHO/SWAN to constrain the SW dynamic pressure at mid to high latitudes (e.g., Izmodenov & Alexashov 2015), yielding ∼25% to ∼40% higher SW dynamic pressure at mid latitudes compared to low and high latitudes. While we cannot argue for or against the use of this data set, we are compelled to use SW speed and density observations from Ulysses observations to verify that the SW dynamic pressure is (on average over time) approximately independent of latitude.

We note, however, that our choice of SW boundary conditions in the MHD simulation does not affect the neutral SW source for the ribbon model. We create a separate, analytically derived neutral SW distribution, described in Section 2.2, to model the source of the PINS that generate ribbon ENAs in the OHS.

2.2. Neutralized SW Source

Following Swaczyna et al. (2016) and Zirnstein et al. (2019a, 2019b), we compute an analytically derived neutral SW distribution, rather than utilize the neutral distribution from our three-dimensional simulation of the heliosphere, since the simulation's neutral grid size is larger than the angular width of the actual neutral distribution outside the heliopause. We summarize the derivation of the neutral SW distribution below.

The neutral SW distribution model uses SW speed and density values derived from interplanetary scintillation (IPS) observations (Sokół et al. 2015). We use the data extracted from a period in time (2000–2009) that is earlier than the IBEX epoch such that we consider the time it takes the supersonic SW to become neutralized, travel to the OHS, and then to propagate back as secondary ENAs. The time period between 2000 and 2009 also accounts for the difference in time for ∼0.7 and 4.3 keV ENAs to experience charge exchange and propagate to 1 au (the range of energies observed by IBEX-Hi; see Table 2 in Zirnstein et al. 2015b). The integral of the neutralized, supersonic SW differential flux, $I_{\rm NSW}$, is

$$\begin{aligned} I_{\rm NSW}(r_{\rm TS},\,v,\,\theta,\,\phi) = \frac{1}{M}\sum_i \int_{r_0}^{r_{\rm TS}} [n_{\rm SW,0,i}(\theta) u_{\rm SW,0,i}(\theta)] \\ \times \left(\frac{r_0}{r_{\rm TS}(\theta,\,\phi)}\right)^2 [n_{\rm H}(r,\,\theta,\,\phi)\sigma_{\rm ex}(v)] \\ \times {\rm e}^{-n_{\rm H}(r,\theta,\phi)\sigma_{\rm ex}(v)r} N(u_{\rm SW,i}(r,\,\theta,\,\phi),\,\delta v|v) \\ \times \frac{1}{m_{\rm p} v}{\rm d}r, \end{aligned} \tag{1}$$

where $u_{\rm SW,0,i}$ and $n_{\rm SW,0,i}$ are the bulk SW speed and density at $r_0 = 1$ au from the IPS SW model (Sokół et al. 2015), v is the neutral SW speed, θ is latitude, ϕ is longitude, i represents the summation index for IPS-derived SW speed and density ($M = 134$ Carrington rotations) such that Equation (1) is time averaged over 2000–2009, $n_{\rm H}(r,\,\theta,\,\phi)$ is the interstellar neutral H density inside the heliosphere extracted from our three-dimensional MHD/kinetic simulation, r is distance from the Sun to the TS $r_{\rm TS}(\theta,\,\phi)$ which we extract from our three-dimensional MHD/kinetic simulation, and $m_{\rm p}$ is mass of protons. We take into account the spread in SW speeds by modeling the distribution N as a Gaussian speed distribution with mean $u_{\rm SW,i}(r,\,\theta)$ and variation $\delta v = 100\,{\rm km\,s^{-1}}$. We note that recent analyses of the charge-exchange cross section ($\sigma_{\rm ex}$) for H–H^+ interactions may need corrections at low energies (Swaczyna et al. 2019; Bzowski & Heerikhuisen 2020), but for our purposes ($\gtrsim$1 keV) the empirical equation from Lindsay & Stebbings (2005) is sufficient.

As discussed in Section 2.1.2, our three-dimensional MHD/kinetic simulation does not reproduce the distance to the TS as inferred from Voyager 1 and 2 crossings, but rather underestimates the TS distances (observed average ∼89 au) by ∼9 au, on average. To compensate for this discrepancy, in Equation (1), we scale $r_{\rm TS}(\theta,\,\phi)$ by a factor of 1.11 in all directions such that the distances compare better to the average distance to the TS from the Voyager 1 and 2 crossings.

The SW speed $u_{\rm SW,i}(r,\,\theta)$ slows with distance r from the Sun due to mass-loading of PUIs. We estimate the effects of this slowing in a manner similar to Swaczyna et al. (2016),

$$\begin{aligned} u_{\rm SW,i}(r,\,\theta,\,\phi) &= u_{\rm SW,0,i}(\theta)\left[1 - \left(1 - \frac{1}{2}\frac{\gamma-1}{2\gamma-1}\right)\right. \\ &\quad \left.\times \frac{r}{\lambda_{\rm ml}(r,\,\theta,\,\phi)}\right], \\ \lambda_{\rm ml}(r,\,\theta,\,\phi) &= [\sigma_{\rm ex}\langle n_{\rm H}(\theta,\,\phi)\rangle + (n_{\rm SW,0,i}(\theta) u_{\rm SW,0,i}(\theta))^{-1} \\ &\quad \times (\nu_{\rm H}\langle n_{\rm H}(\theta,\,\phi)\rangle + 4\nu_{\rm He} n_{\rm He})]^{-1}, \end{aligned} \tag{2}$$

where the adiabatic index $\gamma = 5/3$, the interstellar neutral He density $n_{\rm He} = 0.015\,{\rm cm}^{-3}$ is assumed to be constant with distance, and the photoionization rates for H and He at 1 au are $\nu_{\rm H} = 1.3 \times 10^{-7}\,{\rm s}^{-1}$ and $\nu_{\rm He} = 1 \times 10^{-7}\,{\rm s}^{-1}$ (Sokół et al. 2020). For simplicity we assume $n_{\rm He}$, $\nu_{\rm H}$, and $\nu_{\rm He}$ are constant in time. A notable difference in our method is that $\langle n_{\rm H}(\theta, \phi)\rangle$ is the average neutral H density from our simulation between 1 au and distance r from the Sun, rather than assuming it is a constant value everywhere.

Extending Equation (1) to the OHS, the neutral SW flux as a function of distance r from the Sun becomes

$$I_{\rm NSW}(r, v, \theta, \phi) = I_{\rm NSW}(r_{\rm TS}, v, \theta, \phi)\left(\frac{r_{\rm TS}(\theta, \phi)}{r}\right)^2 \times {\rm e}^{-\int_{r_{\rm HP}}^{r} n_{\rm p}(\mathbf{r}')\sigma_{\rm ex}{\rm d}r'}, \quad (3)$$

where $r_{\rm HP}(\theta, \phi)$ is the radial distance to the heliopause in the MHD simulation. Equation (3) is used as the source of PINS outside the heliopause for our post-processing models of the ribbon in Section 2.3.

2.3. Simulating the Ribbon

2.3.1. Limit of Strong Pitch-angle Scattering

Following our previous work (Zirnstein et al. 2019a, 2019b), we simulate the ribbon in the strong pitch-angle-scattering limit using the methodology from Schwadron & McComas (2013). We briefly summarize the methodology below. We present the distribution of PINS outside the heliopause and the source rate of neutral SW atoms that generate the PINS distribution.

The PINS distribution, f_0, close to $\boldsymbol{B}\cdot\boldsymbol{r} = 0$ where the scattering of ions is strong is

$$f_0(\boldsymbol{r}, v_{\parallel} \leqslant v_A) = S_{\rm NSW}\tau_{\rm ex} + f(z \leqslant z_A). \quad (4)$$

The initial PINS velocity vector parallel to the local ISMF direction, $v_{\parallel}$, is used to define the retention region, depending on whether it is smaller than the local Alfvén speed $v_{\rm A}$. The retention region as defined by Schwadron & McComas (2013) (see their Figure 3) is the region in the OHS where strong pitch-angle scattering of PINS occurs. PINS that are generated in this region by charge exchange have initial parallel speeds smaller than the local Alfvén speed, and experience significant scattering. Since PINS generated in the OHS originate from radially propagating neutral SW, the retention region is centered on directions near $\boldsymbol{B}\cdot\boldsymbol{r} = 0$, where the angular width of the retention region as a function of distance from the heliopause depends on the local Alfvén speed (i.e., location $\boldsymbol{r}$ is within the retention region if $|\boldsymbol{v}_{\rm NSW}\cdot\boldsymbol{B}|/|\boldsymbol{B}| \leqslant v_{\rm A}$, where $\boldsymbol{v}_{\rm NSW}$ is the radial neutral SW velocity). $S_{\rm NSW}$ is the source rate of neutral H atoms produced in the SW (see Equation (7) below). The local ion-neutral charge-exchange rate is $1/\tau_{\rm ex} = n_{\rm H}(\boldsymbol{r})\sigma_{\rm ex}(v)v$. The term f determines the enhancement of ions near $\boldsymbol{B}\cdot\boldsymbol{r} = 0$ via the streaming of ions into the retention region, given as

$$f(z \leqslant z_A) = a\{\exp[-k_+(z - z_{\rm A})] - \exp[-k_-(z - z_{\rm A})]\}, \quad (5)$$

where the solutions for the amplitude a and wavenumbers $k_{\pm}$ are shown in Schwadron & McComas (2013) (however, note the typo in their Equation (A16), which is fixed in Zirnstein et al. 2019a). As described by Schwadron & McComas (2013), f is defined as a function of local distance z away from $\boldsymbol{B}\cdot\boldsymbol{r} = 0$ along the ISMF line, i.e., $z = r\tan(\pi/2 - \cos^{-1}(|\boldsymbol{v}_{\rm NSW}\cdot\boldsymbol{B}|/|\boldsymbol{v}_{\rm NSW}||\boldsymbol{B}|))$. For $z > z_{\rm A}$ (solving z for $|\boldsymbol{v}_{\rm NSW}\cdot\boldsymbol{B}|/|\boldsymbol{B}| > v_{\rm A}$), the boundary of the retention region where the parallel speed of PINS exceeds the Alfvén speed, a different condition is imposed below. As shown by Schwadron & McComas (2013) and Zirnstein et al. (2019a), it is the term f that produces an enhanced PINS density in the retention region, which depends on the rates of scattering and charge exchange.

For distances $z > z_{\rm A}$, the PINS distribution is

$$f_0(\boldsymbol{r}, v_{\parallel} > v_A) = S_{\rm NSW}(\tau_{\rm ex} - \tau_{\rm l}), \quad (6)$$

where $1/\tau_{\rm l} = 2/\tau_{\rm s} + 1/\tau_{\rm ex}$, and $\tau_s = 3/8\int_{-1}^{1}(1 - \mu^2)^2/(D_{\mu\mu})d\mu$. The pitch-angle diffusion coefficient $D_{\mu\mu}$ is calculated from the case of gyro-resonant particle scattering in parallel-propagating Alfvén waves and fast magnetosonic waves (e.g., Schlickeiser 1989; Gamayunov et al. 2010). The pitch-angle scattering time ($\tau_{\rm s}$) and the charge-exchange time ($\tau_{\rm ex}$) determine the level of scattering outside the retention region and whether or not ENAs can be observed (i.e., only ENAs produced from PINS that scatter across 90° when outside the retention region can be observed by IBEX). When $1/\tau_{\rm s} \gg 1/\tau_{\rm ex}$, PINS will quickly scatter in pitch angle (forming an isotropic shell distribution) before becoming secondary ENAs. This creates a uniform background of ENA fluxes in all directions of the sky that can be observed by IBEX, but at a relatively low intensity compared to the peak ribbon flux. When $1/\tau_{\rm s} \ll 1/\tau_{\rm ex}$, PINS will not scatter significantly before experiencing charge exchange: these PINS cannot produce ENAs observed by IBEX. We present results for the limit $1/\tau_{\rm s} \ll 1/\tau_{\rm ex}$, as in our previous work, to test how it affects the geometry of the ribbon.

Finally, $S_{\rm NSW}$, is given by

$$S_{\rm NSW}(\boldsymbol{r}, v) = \frac{I_{\rm NSW}(\boldsymbol{r}, v)}{4\pi v^2} m_{\rm p} n_{\rm p}(\boldsymbol{r})\sigma_{\rm ex}v, \quad (7)$$

where $I_{\rm NSW}$ is calculated using Equation (2).

2.3.2. Limit of Weak Pitch-angle Scattering

In this section, we summarize the methodology applied in our previous work to simulate the ribbon in the limit of weak pitch-angle scattering (Zirnstein et al. 2018a, 2019b). The ribbon in the weak-scattering limit is calculated from a backward integration model, where we solve the PINS guiding-center motion backward in time, starting from the point of ribbon ENA creation in the OHS (position $\boldsymbol{r}$) with speed v equal to the speed of an ENA we aim to simulate, and initial pitch-angle φ aligned with the IBEX detector look direction. In this limit, the physical processes controlling the distribution of PINS outside the heliopause (in addition to their source term) are parallel streaming, magnetic mirroring, advection, and betatron acceleration. We have shown previously (Zirnstein et al. 2018a) that advection and betatron acceleration due to the advection of PINS into the compressed ISMF in the OHS do not significantly affect the PINS distribution. Therefore, advection and betatron acceleration are not included in our model of the ribbon in the weak-scattering limit. Thus, the

relevant equations of motion are given as

$$\frac{d\boldsymbol{r}}{dt} = v_{\parallel}\frac{\boldsymbol{B}}{|\boldsymbol{B}|},$$
$$\frac{dv_{\parallel}}{dt} = -\frac{\mu}{m_p}\frac{\partial B}{\partial s_{\parallel}}, \quad (8)$$

where μ is the (adiabatic invariant) magnetic moment, $\boldsymbol{B}$ is the local MHD magnetic field vector, $v_{\parallel}$ is the particle speed parallel to the magnetic field, and $s_{\parallel}$ is the step size along the magnetic field. Equation set (8) is solved with a fourth-order Bulirsch-Stoer routine with adaptive fifth-order accuracy achieved by step doubling, with step sizes constrained such that the local truncation error is less than 10^{-5}. We note that our method does not simulate a large number of test particles with randomized positions and velocities, but rather the backward integration of a single guiding center starting from position $\boldsymbol{r}$ in the OHS with pitch angle and energy coinciding with an ENA emitted from that position. Once the guiding-center motion is tracked backward in time for a sufficiently long time (see description below), we take another step farther along the IBEX LOS by a fraction of the local MHD grid size and repeat the process. More details on this procedure can be found in Zirnstein et al. (2018a).

As we solve the guiding-center motion of a PINS starting from position $\boldsymbol{r}$ in the OHS, we integrate the production rate of PINS from the local neutral SW source at each guiding-center step and weight the probability for the PINS to survive charge exchange until reaching position $\boldsymbol{r}$ (i.e., the farther away the guiding-center step is from the start position $\boldsymbol{r}$, the less chance a PINS has of making it to position $\boldsymbol{r}$). The PINS distribution in the weak-scattering limit is therefore

$$f_0(\boldsymbol{r}, v) = \int_0^{t_{\max}} W(t)\left[\frac{1}{\Delta\varphi}\int_{-\Delta\varphi/2}^{+\Delta\varphi/2}\left(\frac{1}{2\pi}\right.\right.$$
$$\left.\left.\times\int_0^{2\pi} S_{\rm NSW}(\boldsymbol{r}, v, \Omega, \varphi)\tau_{\rm ex}\,d\Omega\right)d\varphi\right]dt,$$
$$W(t) = \frac{\exp(-t/\tau_{\rm ex})}{\int_0^{t_{\max}}\exp(-t'/\tau_{\rm ex})dt'}, \quad (9)$$

where $W(t)$ represents a function used to weight the survival probability of PINS traveling along the ISMF before charge exchange (i.e., before reaching position $\boldsymbol{r}$). The total time for solving the guiding-center motion is $t_{\max}$. Ideally, $t_{\max} = \infty$; however, due to computational limitations, this is unfeasible to simulate. Therefore, we set $t_{\max} = 3\tau_{\rm ex}$, where $t_{\max}$ is sufficiently larger than $\tau_{\rm ex}$ such that the majority of possible particles are accounted for ($1 - \exp(-3\tau_{\rm ex}/\tau_{\rm ex}) \cong 0.95$). The total number of PINS that could contribute to ENAs observed by IBEX at position $\boldsymbol{r}$ are thus integrated by solving Equation set (9), where the guiding-center-motion time step is dt and, at each position along the guiding-center trajectory, we integrate over the local neutral source $S_{\rm NSW}$ multiplied by the local charge-exchange time $\tau_{\rm ex}$ at gyro-phase Ω of ions defined by the local pitch-angle φ determined from Equation (8).

Similar to our previous work, we assume that a small amount of pitch-angle scattering ($\Delta\varphi$) around the nominal pitch angle (φ) occurs. We make this assumption since particle-in-cell simulations (Florinski et al. 2016) suggest that, in the warm VLISM plasma, the PINS distribution may slightly widen in pitch angle but otherwise remain stable for a significant fraction of time, until charge exchange occurs. Therefore, Equation (9) also includes a normalized integration across a small window around φ, where $\Delta\varphi = 5°$.

The function $S_{\rm NSW}$ is slightly different in the weak-scattering limit,

$$S_{\rm NSW}(\boldsymbol{r}, v, \Omega, \varphi) = I_{\rm NSW}(\boldsymbol{r}, v)m_{\rm p}n_{\rm p}(\boldsymbol{r})\sigma_{\rm ex}v$$
$$\times\left[\frac{1}{\pi\delta v_{\rm tr}^2(r)}e^{-\left(\frac{v_{\rm tr}}{\delta v_{\rm tr}(r)}\right)^2}H(90°\right.$$
$$\left.-\cos^{-1}(\hat{\boldsymbol{v}}_{\rm p}\cdot\hat{\boldsymbol{r}}))\right],$$
$$v_{\rm tr} = v\sin(\cos^{-1}(\hat{\boldsymbol{v}}_{\rm p}\cdot\hat{\boldsymbol{r}})),$$
$$\delta v_{\rm tr}(r) = \sqrt{\frac{2k_{\rm B}T_{\rm tr,TS}}{m_{\rm p}}\left(\frac{r_{\rm TS}}{r}\right)^2}, \quad (10)$$

where $\boldsymbol{v}_{\rm p} = \boldsymbol{v}_{\rm p}(\Omega, \varphi)$ is the desired PINS velocity vector (with magnitude v). The neutral SW source has a transverse thermal spread, $\delta v_{\rm tr}$, which is defined initially at the TS as $T_{\rm tr,TS} = 5000$ K, and then propagated via adiabatic expansion as a function of distance from the Sun (for more details, see Florinski & Heerikhuisen 2017).

2.3.3. Differential ENA Flux

After solving for the PINS distribution in the OHS as shown in Sections 2.3.1 and 2.3.2, we can calculate the differential ENA flux from our simulated ribbon. This is given as

$$J(\theta, \phi, v) = \int_{r_{\rm HP}}^{r_{\rm OB}}\frac{1}{m_{\rm p}}f_0(\boldsymbol{r}_{\rm LOS}, v)v^2n_{\rm H}(\boldsymbol{r}_{\rm LOS})$$
$$\times\sigma_{ex}P(\boldsymbol{r}_{\rm LOS}, v)dr_{\rm LOS}, \quad (11)$$

where $r_{\rm HP}$ is the simulation heliopause distance, $r_{\rm OB} = 700$ au is the outer boundary distance (beyond $r_{\rm OB}$ the ENA source is negligible), $\boldsymbol{r}_{\rm LOS}$ is the IBEX LOS position vector, and $P(\boldsymbol{r}_{\rm LOS}, v)$ is the survival probability of ENAs from their point of creation to the TS. We do not include the probability of ENA loss at distances within the TS since we compare our results to the survival-probability-corrected IBEX data.

3. Analysis and Results

To analyze the geometric properties of our simulated ribbon results, we employ similar analysis techniques used by Funsten et al. (2013); Zirnstein et al. (2016a), and Dayeh et al. (2019). We first simulate the ribbon at each IBEX-Hi energy passband in a ribbon-centered frame, where the center is set as a function of energy to the centers derived by Dayeh et al. (2019). The centers are (217.°41, 44.°36), (219.°72, 41.°5), (220.°51, 39.°96), (218.°08, 38.°44), and (214.°68, 34.°13) for energy bins centered on 0.71, 1.11, 1.74, 2.73, and 4.29 keV, respectively. The $+z$-axis is aligned with these directions, and the coordinate system is rotated about the z-axis such that the $+x$-axis crosses the VLISM inflow direction (labeled "nose" in Figure 1) given by (255.°7, 5.°1).

Before we analyze the geometric properties of the simulated ribbon results, we make three modifications to better mimic realistic observations. First, our simulation does not include the GDF, whereas IBEX observations include the GDF behind and

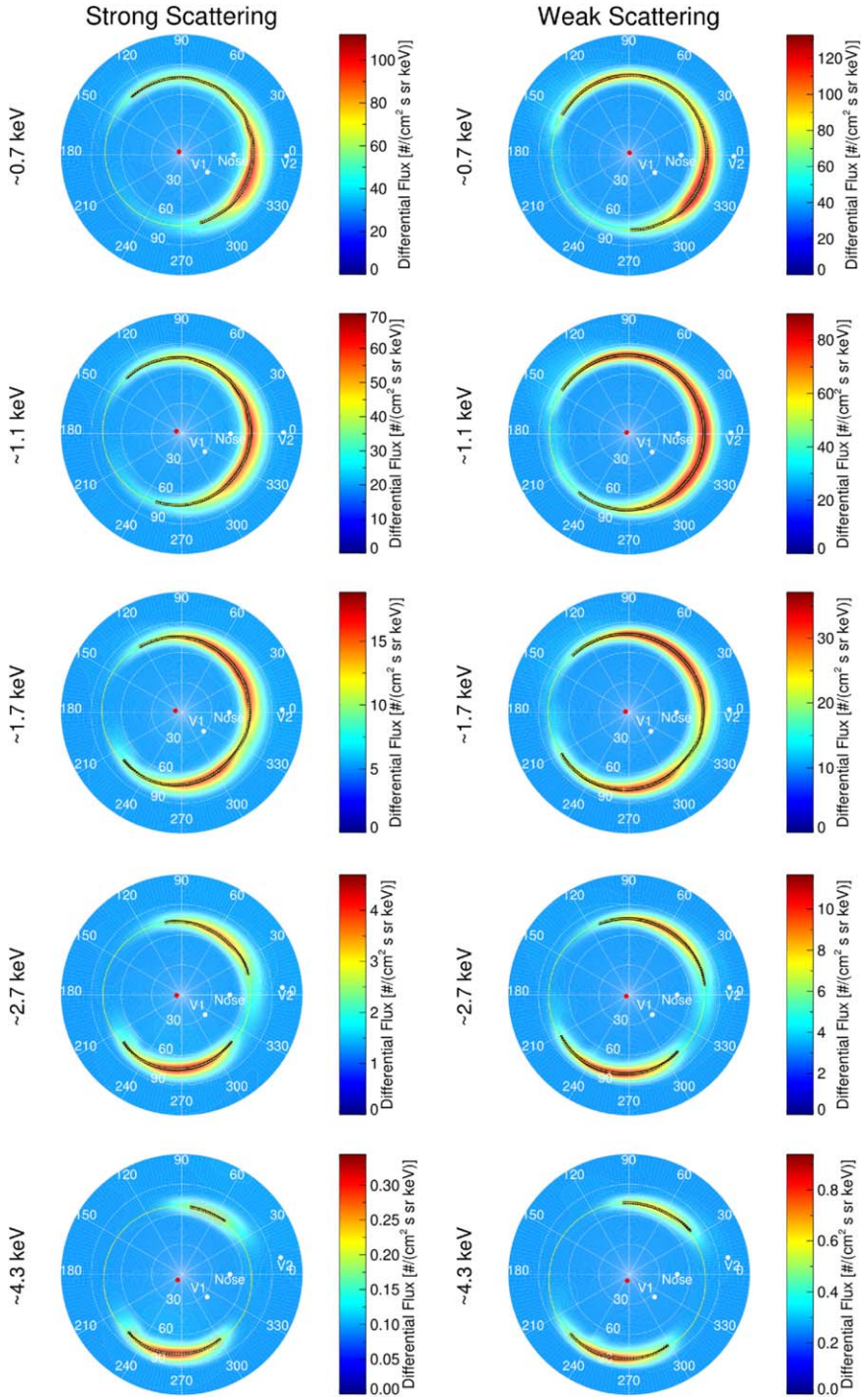

Figure 1. Simulated ribbon-centered maps at each IBEX-Hi energy passband (rows) for each ribbon model (columns). Note that we added a background flux proportional to 40% of the peak ribbon flux in each map. The locations of the peak ribbon flux as defined by Equation (13) are shown as black dots. The 1σ uncertainties of the peak locations are shown as gray bars emanating from the black dots (both + and −1σ). The fits to the ribbon peaks are shown as yellow circles and the centers of the fits are red dots. Note that the color bar ranges are unique to each panel to highlight the flux ranges.

around the ribbon. A smooth background of flux should not affect the results significantly, however if we attempt to fit functions to data at pixels with zero (or near-zero) flux, this may significantly affect the results. Therefore, we add a constant (independent of direction in the sky) background of flux to the simulation results as a function of energy, namely, 40% of the peak ribbon flux in each simulated all-sky map. The second modification is that we emulate realistic uncertainties of the simulation results, similar to IBEX measurements. We estimate uncertainties by relating the simulated flux in each pixel, J, to IBEX-Hi's instrument response, such that (e.g., Funsten et al. 2009a)

$$J(E) = \frac{C(E)}{EG(E)},$$
$$\sigma_J(E) = \sqrt{\frac{J(E)}{EG(E)\tau(E)}}, \quad (12)$$

where C is count rate, E is the central energy of the ESA passband, G is the energy-dependent geometric factor of IBEX-Hi, τ is the time exposure (which we assume is constant over the sky), and σ_J is the uncertainty of the flux. We calculate the all-sky average time exposure for each ESA passband over the first nine years of IBEX observations, corresponding to the time period of IBEX observations we compare our results to Dayeh et al. 2019, yielding $\tau = 1303$, 2217, 1999, 2060, and 1895 s for ESA 2 through 6, respectively. Equation (12) allows us to emulate uncertainties for our simulation results as a function of energy and flux in each pixel. We note, however, that scaling σ_J by the geometric factor and time exposure do not affect the fitting process since they are constants over the entire sky. The most important variable in Equation (12) is assuming the uncertainty σ_J is proportional to $\sqrt{J(E)}$, emulating realistic measurements. The final modification is that we "smooth" the simulation results in angular direction, as we have done in our previous work, by the IBEX-Hi collimator response function (Funsten et al. 2009a). The angular response function is well approximated by a triangular function with maximum transmission in the pixel center and zero transmission $\sim 7°$ from the pixel center.

Next, we fit a skew normal distribution function, F, to the simulation results in each azimuthal sector across the ribbon (angle around the ribbon center) given by

$$F(\phi) = A_S + B_S \times \exp\left(-\frac{(\phi - \phi_c)^2}{2\sigma_S^2}\right) \times \mathrm{erfc}\left(-\alpha\frac{\phi - \phi_c}{\sqrt{2}\,\sigma_S}\right), \quad (13)$$

where A_S is a constant background, B_S is the skew normal amplitude, ϕ is the angular distance from the pole (or plot center), ϕ_c is the angular distance from the pole to the peak of the exponential (non-skewed) distribution, σ_S is the standard deviation, α is the skewness parameter, and erfc() is the complementary error function. Similar to Zirnstein et al. (2016a), we (1) fit Equation (13) to a 42° polar range of pixels across the ribbon (the simulated pixels are $2° \times 2°$ in size), with the range centered on the pixel of maximum flux, (2) ignore azimuthal regions between 150° and 210° which are close to the heliotail and are independent of the ribbon's source, and (3) ignore fits where $B_G/|A_G| < 0.2$, i.e., regions of low peak flux compared to the background. The best-fit results are found using Levenberg-Marquardt least-squares minimization (Markwardt 2009).

With these criteria, we find the angular distance from the center of the ribbon peak in each 2° azimuthal sector, ϕ_c, and its uncertainty, $\sigma_{\phi c}$. We note that the peak of the skew normal distribution does not have an analytic expression. Therefore, we find the peak by finding the root of the derivative of Equation (13), i.e., $F'(\phi) = 0$, using an optimal Muller's method (e.g., Press et al. 2007). The 1σ uncertainty of the peak location is found by manually propagating the uncertainties of the fluxes in each pixel of the azimuthal sector, i.e.,

$$\sigma_{\phi c} = \sqrt{\sum_i (\partial\phi_{c,i}/\partial J)^2 \sigma_{J,i}^2} \cong \sqrt{\sum_i (\Delta\phi_{c,i})^2}\,, \quad (14)$$

where $\Delta\phi_{c,i} = \phi_c - \phi_{c,i}$. This is done by adding the 1σ uncertainty of the fluxes to each pixel individually at index i, finding the new peak location $\phi_{c,i}$ through fitting Equation (13) to the altered data, difference the fitted peak $\phi_{c,i}$ from the nominal value ϕ_c, and repeat for all pixels. Summing over all combinations yields the total uncertainty in Equation (14).

Next, we fit a circle to the peak locations of the ribbon peak (separately for each energy and ribbon model) using Levenberg-Marquardt least-squares minimization. The uncertainties in ϕ_c are used as weights in the circle fits. With the circle fits, we find the center of the ribbon and its mean radius as a function of energy. Their uncertainties are calculated from the standard deviation of the locations of ϕ_c along the circle from the mean radius.

3.1. Comparison of Ribbon Centers with Observations

The simulated ribbon-centered maps are shown in Figure 1 along with their fits. Similar to our previous work, the ribbon flux is concentrated near the nose direction/ecliptic plane at the lowest energy (0.7 keV), and then splits into low- and high-latitude emissions away from the nose at higher energies (>2 keV). It is also worth pointing out that the ribbon intensities predicted by the models are different (see also Zirnstein et al. 2019a), and the weak-scattering model compares better to the separated ribbon fluxes from Schwadron et al. (2014b). The centers of the ribbon as a function of energy are shown in Figure 2, for IBEX data averaged over 9 yr of observations (Dayeh et al. 2019) and our simulation results. The results are also listed in Table 1. We show the ribbon centers as a function of energy and their mean. The uncertainties are derived as a combination of the propagated uncertainty of the mean and the statistical uncertainty about the mean (see Appendix C in Zirnstein et al. 2016b).

It is immediately clear that the spread of the ribbon centers in longitude/latitude as a function of energy is much larger in the IBEX data than in our simulation results. The reason for this is not immediately clear, although several differences in our simulations may be the cause of this discrepancy. First, our results do not self-consistently simulate the GDF, rather we include a constant background to improve the accuracy of our fitting around pixels with near-zero fluxes. A diffuse but nonuniform GDF may influence the fitting procedure in the data. Second, our simulation is performed on a $2° \times 2°$ angular grid, whereas the IBEX data are in a $6° \times 6°$ angular grid. Potentially it is possible that the coarser grid can shift the ribbon centers in energy, but perhaps not systematically in one direction. Swaczyna et al. (2016) produced a larger angular spread between ribbon centers from their simplified ribbon model, though they did not include the three-dimensional draping effects of the ISMF around the heliosphere. Our model includes the ISMF draping, thus the reason for the discrepancy between our results and the data is not clear.

In general, the simulation results show a systematic trend downward in ecliptic latitude as a function of increasing energy, for both pitch-angle-scattering limits. This is qualitatively similar to IBEX observations: the IBEX ribbon centers also show a shift in longitudinal trend from right to left at lower ENA energies. However, at higher ENA energies, the observed ribbon centers decrease in longitude as latitude decreases, which is not reproduced in our simulations. This shift was suggested by Dayeh et al. (2019) to be a result of the combination of (1) the draping of the ISMF around the

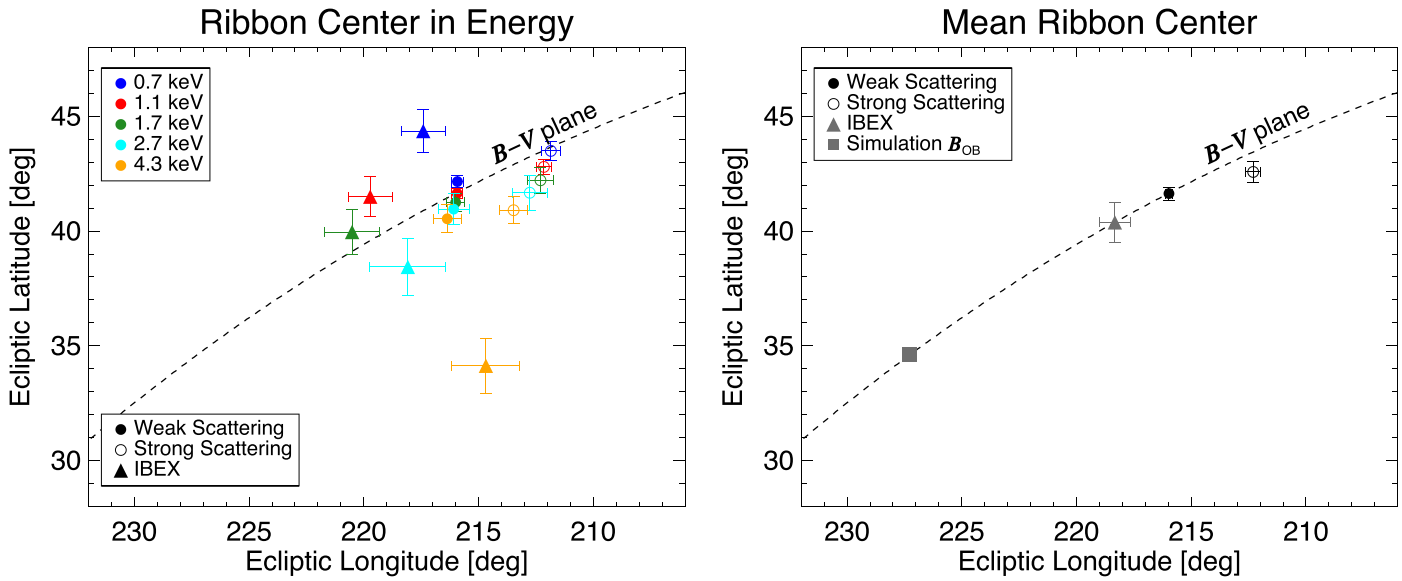

Figure 2. Comparison of the ribbon centers from IBEX observations and our simulation results. We also show the *B*–*V* plane defined by the simulation's pristine ISMF direction far from the influence of the heliosphere (i.e., the outer boundary ISMF direction, "$\boldsymbol{B}_{\rm OB}$") and the VLISM inflow direction.

Table 1
Simulation Results of the IBEX Ribbon Center and Radius

Model/Data	ENA Energy (keV)	Center Longitude, Latitude (°)	Center Uncertainty (°)	Radius (°)	Radius Uncertainty (°)	Mean Center Longitude, Latitude (°)	Mean Radius (°)
Weak Scattering	0.7	(215.92, 42.16)	0.28	76.95	0.28	(215.97 ± 0.16, 41.64 ± 0.28)	77.01 ± 0.20
	1.1	(215.93, 41.65)	0.23	76.90	0.23		
	1.7	(216.00, 41.25)	0.39	77.02	0.39		
	2.7	(216.08, 40.96)	0.68	77.35	0.68		
	4.3	(216.36, 40.54)	0.61	77.83	0.61		
Strong Scattering	0.7	(211.85, 43.49)	0.42	73.52	0.42	(212.30 ± 0.33, 42.58 ± 0.47)	73.34 ± 0.22
	1.1	(212.15, 42.80)	0.32	73.28	0.32		
	1.7	(212.30, 42.21)	0.56	73.17	0.56		
	2.7	(212.77, 41.67)	0.76	73.21	0.76		
	4.3	(213.47, 40.91)	0.60	73.48	0.60		
IBEX[a]	0.7	(217.41, 44.36)	(0.95, 0.93)	75.10	1.06	(218.33 ± 0.68, 40.38 ± 0.88)	74.81 ± 0.65
	1.1	(219.72, 41.50)	(0.95, 0.87)	73.19	0.86		
	1.7	(220.51, 39.96)	(1.19, 1.00)	73.36	1.01		
	2.7	(218.08, 38.44)	(1.66, 1.24)	75.17	1.28		
	4.3	(214.68, 34.13)	(1.48, 1.19)	78.86	1.48		

Note.
[a] IBEX data are averaged over 2009–2017, therefore the uncertainties in the IBEX ribbon centers are different in longitude and latitude before averaging over energy. From Dayeh et al. (2019).

heliopause affecting the lower energy ENA results (Zirnstein et al. 2016a) and (2) the latitudinal SW structure affecting the higher energy ENA results (Swaczyna et al. 2016). Our simulation results, which do account for both the draping of the ISMF and the latitudinal SW structure, do not show a shift in the trend of ribbon centers at higher ENA energies. Rather, the simulated ribbon centers appear to follow a single path that is approximately between the *B*–*V* plane and the solar meridional plane (a line of constant longitude). Note also that our simulation results are not clustered as close as our previous study (Zirnstein et al. 2016a) where we did not include the latitudinal SW structure. The discrepancy between the spatial location of the ribbon centers as a function of ENA energy between the observations and our simulations will be analyzed in more detail in a future study.

The mean ribbon centers, averaged over ENA energy, are shown in the right panel of Figure 2. All ribbon centers for both the IBEX data and the simulation results in both pitch-angle scattering limits lie near the *B*–*V* plane. Note that the *B*–*V* plane is defined by a great plane intersecting the simulation's pristine

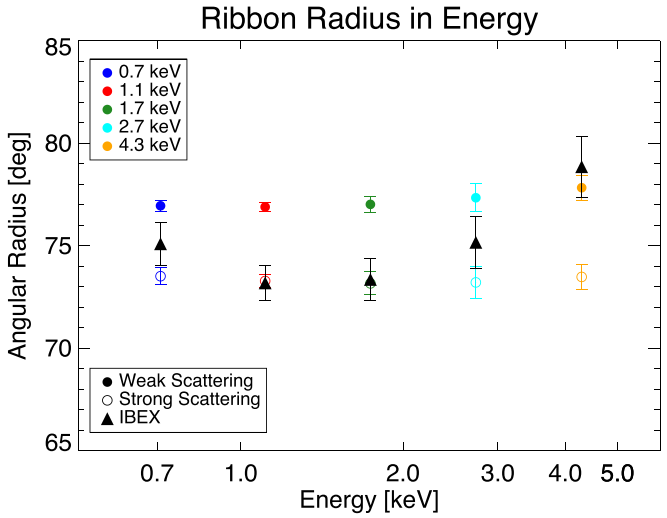

Figure 3. Comparison of the ribbon radii from IBEX observations and our simulation results.

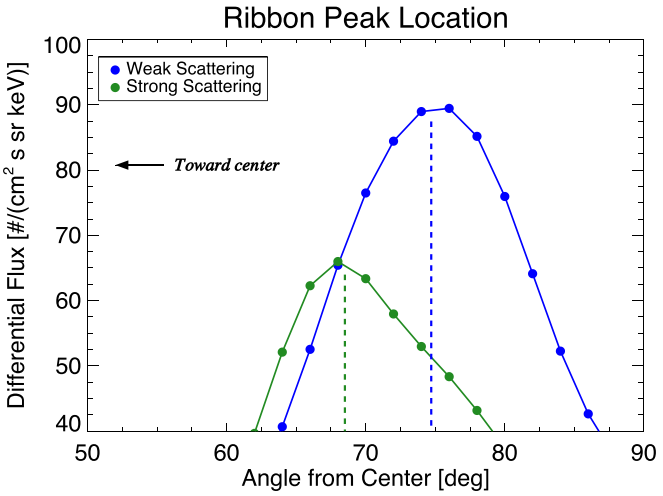

Figure 4. Simulated ribbon flux at 1.1 keV in the strong- and weak-scattering limits as a function of angle from the polar plot centers defined in Figure 1. We extracted fluxes within ±5° of the 0° azimuth line. Also shown is the location of the peaks derived from the skew normal fits (dashed lines).

ISMF direction far from the influence of the heliosphere (Zirnstein et al. 2016b) and the inflow direction of the VLISM (McComas et al. 2015). Therefore, regardless of the pitch-angle-scattering rates influencing the structure of the ribbon, the center of the ribbon still lies close to the *B*–*V* plane. However, the pitch-angle scattering of particles does change the location of the mean ribbon center along the *B*–*V* plane, producing an offset of ∼3° between the different scattering limits. The reason for this offset between the different simulated scattering limits is explained in more detail in Section 3.2.

3.2. Comparison of Ribbon Radii with Observations

Figure 3 compares the ribbon radius results between IBEX data and our simulation results. First, there is a clear difference in the ribbon radius between the weak and strong-scattering simulation results. The weak-scattering model produces a consistent increase in ribbon radius at each ENA energy, most of which are statistically larger than IBEX observations. However, the strong-scattering model reproduces the IBEX ribbon radius at 1.1, 1.7, and nearly 2.7 keV, but not at the lowest (0.7 keV) and highest (4.3 keV) energies. A possible reason for this is that our model does not include (1) neutralized interstellar PUIs from the supersonic SW and (2) neutralized PUIs from the IHS, both of which can make a significant contribution to the ribbon flux at the highest energy passband. Both of these contributions were discussed by Schwadron & McComas (2019) as important contributions to the ribbon at higher energies (see their Figures 2 and 3). Thus, this may explain the discrepancy between our model and the data at 4.3 keV. However, the small discrepancy at 0.7 keV is still not explained, although it may be due to the lower statistical accuracy of the data at this low energy or uncertainties in our simulated neutral SW distribution. The consistency between our strong-scattering results for the ribbon radius and the IBEX data suggest, at least at the middle three energies, that the mechanism of strong pitch-angle scattering of particles outside the heliopause may be responsible for the IBEX ribbon's origin.

The reason why the simulated ribbon centers and radii are different for the strong and weak pitch-angle scattering limits is related to the distances from the Sun where the majority of the ribbon fluxes are originating. As shown by Zirnstein et al. (2019a), the ribbon in the strong-scattering limit is concentrated in the center of the retention region near $\boldsymbol{B} \cdot \boldsymbol{r} = 0$ and close to the heliopause, whereas the weak-scattering model ribbon is spread farther out from the heliopause. This, effectively, moves the ribbon peak closer toward the nose in the strong-scattering limit, and thus moves the ribbon center farther away from the nose. Figure 4 illustrates this in more detail, which shows the ribbon peaks in each model along the *B*–*V* plane. The shift in the peak locations is primarily responsible for the difference in ribbon radius, and less so in the difference in ribbon centers. As discussed by Zirnstein et al. (2019a), the skewness of the ribbon peak in the strong-scattering model, where the ribbon is steeper on the side toward the ribbon center, is opposite of the results found by Funsten et al. (2013).

3.3. Potential Effects on the Pristine ISMF

In Sections 3.1 and 3.2, we showed that the ribbon centers for the weak-scattering model are closer to that observed by IBEX but the ribbon radii for the strong-scattering model are closer to the data. This two-sided result complicates our goal to determine which physical scenario is more likely, but also suggests that the pristine ISMF implemented in our simulation, $\boldsymbol{B}_{\rm OB}$, in fact may be slightly different than what was derived by Zirnstein et al. (2016b), if one of the ribbon models presented in this study is more correct.

While it is beyond the scope of this study to rederive the pristine ISMF for our two ribbon models using the same methodology as Zirnstein et al. (2016b), we can estimate the ISMF required to produce better matches between the simulated and observed ribbon geometries. Based on prior studies, we first note that both the strength and direction of the ISMF affect the location of the center of the ribbon (Zirnstein et al. 2016b) and the radius of the ribbon (Grygorczuk et al. 2011; Heerikhuisen & Pogorelov 2011; Ratkiewicz et al. 2012; Zirnstein et al. 2016b). To first order, we can estimate the direction of the ISMF required to match the simulations results with IBEX ribbon center by assuming the direction of the pristine ISMF, $\boldsymbol{B}_{\rm OB}$, can be shifted along the *B*–*V* plane by the

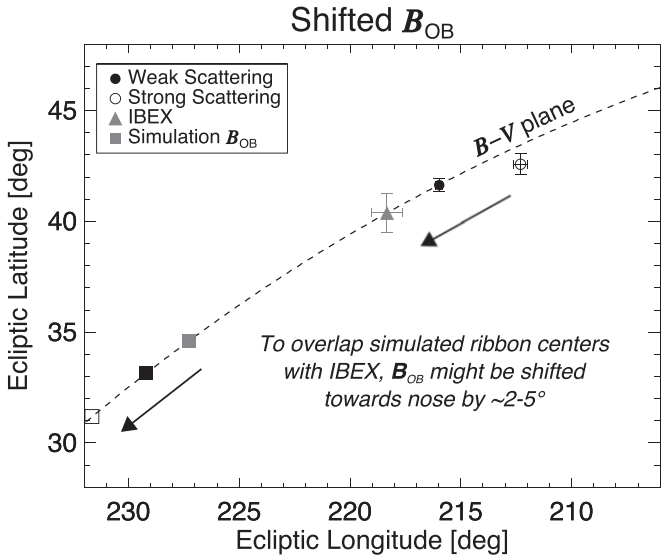

Figure 5. Illustration of the directions for the pristine ISMF ($\boldsymbol{B}_{\rm OB}$) shifted along the *B–V* plane in order to overlap the simulated ribbon centers for the weak and strong-scattering models with the observed IBEX ribbon center. We calculated the directions for the ISMF ($\boldsymbol{B}_{\rm OB}$) for each model as an angular shift along the *B–V* plane by the angles separating the model and data ribbon centers.

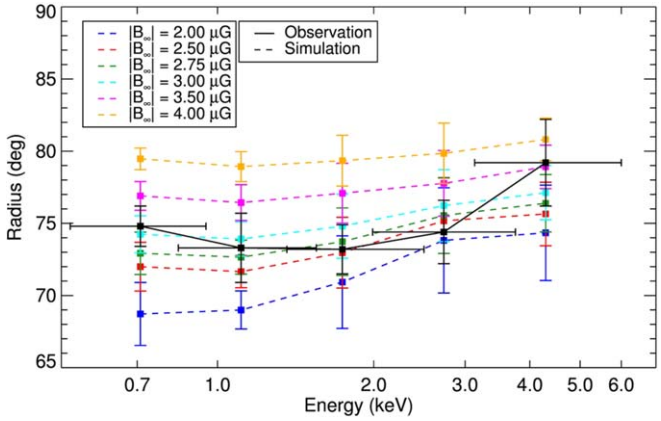

Figure 6. Simulated ribbon radius from Zirnstein et al. (2016a). The simulation of the ribbon is based on the "partial shell" model from Heerikhuisen et al. (2010), and the observations are derived from the first three years of IBEX observations from Funsten et al. (2013). Reproduced from Zirnstein et al. (2016a) with permission from the AAS.

angular separation of each simulated ribbon center from the observed ribbon center. This is illustrated in Figure 5. Note that the direction of the pristine ISMF ($\boldsymbol{B}_{\rm OB}$) does not change more than $\sim5°$ based on our simulation results. This demonstration assumes there is no change in the magnitude of $\boldsymbol{B}_{\rm OB}$, otherwise the angular shift would likely be less significant.

The radius of the ribbon appears largely to be affected by the magnitude of the ISMF. Even with the same ribbon center, a larger magnetic field strength produces a larger ribbon radius (e.g., Heerikhuisen et al. 2014, see Figure 2 in Zirnstein et al. 2016b, reproduced here in Figure 6). Our simulation results in Figure 3 suggest that, if the strong-scattering model is correct, then the ISMF magnitude need not change, and only a small shift in the pristine ISMF direction is necessary to approximately match IBEX observations (at least for the three middle energies). However, if the weak-scattering model is correct, then the magnitude must decrease. Our prior results from Zirnstein et al. (2016b), shown here in Figure 6, suggest that a change in pristine ISMF magnitude is more significant at lower ENA energies than at higher energies. Taking the results in the middle of the ENA spectrum (1.7 keV) from Zirnstein et al. (2016b), the ribbon radius decreases by $\sim4°/\mu$G. Our simulated ribbon radius for the weak-scattering model at 1.7 keV is $\sim5°$ larger than the observed ribbon (with $\sim2°$ uncertainty). This suggests that the pristine ISMF magnitude may be smaller by ~1.25 μG. Therefore, in order for the weak-scattering model to be the IBEX ribbon's true origin mechanism, the ISMF magnitude may be closer to 2 μG rather than 3 μG, meaning that the ISMF direction must be shifted along the *B–V* plane to compensate for a smaller ISMF magnitude.

However, we note that a pristine ISMF magnitude as small as ~2 μG appears highly unlikely based on prior models and analyses of observations of the SW-VLISM interaction, e.g., ion pressures from IBEX ENAs (e.g., Schwadron et al. 2011), TS asymmetries due to the ISMF and solar variations (e.g., Pogorelov et al. 2007, 2013, 2017a; Ratkiewicz & Grygorczuk 2008; Opher et al. 2009), compression of the ISMF outside the heliopause and comparison with Voyager observations (e.g., Zirnstein et al. 2016b; Pogorelov et al. 2017b; Izmodenov & Alexashov 2020), tilt of the port and starboard heliotail lobes (e.g., Zirnstein et al. 2017), Lyα absorption profiles (Zank et al. 2013), and TeV galactic cosmic ray anisotropies (e.g., Schwadron et al. 2014a; Zhang et al. 2020). With these results, it appears more likely that strong pitch-angle scattering is responsible for the IBEX ribbon's geometry. A more self-consistent analysis of the pristine ISMF required to match the strong and weak-scattering models with the IBEX ribbon will be performed in a future study.

3.4. Effects from Interstellar Helium

We note that the interstellar proton density of 0.09 $\rm cm^{-3}$ used in our analysis up to now is effectively the total plasma density, not just that of protons, in terms of dynamic pressure. The inclusion of interstellar He ions as derived from IBEX-Lo observations (Bzowski et al. 2019) suggests that the effective He ion density is ~0.009 $\rm cm^{-3}$ and thus the proton density should be smaller, approximately 0.054 $\rm cm^{-3}$. A smaller proton density implies that the H–H^+ charge-exchange rate is smaller, and that the interstellar neutral H density must be smaller to compensate for the smaller filtration rate of neutral H through the heliosphere. In this section, we analyze how the inclusion of interstellar He may affect the geometric properties of the ribbon.

Currently, most three-dimensional simulations of the heliosphere do not self-consistently account for the presence of interstellar He ions and neutrals and their dynamical effects on the SW-VLISM interaction, although their presence has been studied in a more ad-hoc manner (e.g., Izmodenov et al. 2003; Müller & Zank 2004; Kubiak et al. 2014). Bzowski et al. (2019) recently derived the ionization degree of interstellar He based on IBEX-Lo observations, finding an interstellar He^+ density of $\sim9\times10^{-3}$ $\rm cm^{-3}$ and ionization degree of 0.37. This implies an interstellar proton density of $\sim5.4\times10^{-2}$ $\rm cm^{-3}$, which is 60% of the total plasma density used in our MHD simulation (note that the MHD simulation used to derive the interstellar densities by Bzowski et al. (2019) is the same as that used in our study). The reason for the scaling of 60% is due to the fact that the relative abundance of interstellar He^+ to H^+ is $\sim10\%$, but the mass of He is four times that of H. Thus,

approximately 40% of the dynamic pressure of the VLISM plasma is from He^+. The dynamic pressure in our current MHD simulation must remain the same to maintain the pressure on the heliopause and thus its distance from the Sun.

Since the charge-exchange ionization rate between H (H^+) and He^+ (He) is much smaller than that between H and H^+, we can mimic the presence of interstellar He in our ribbon models by scaling our simulation's interstellar H^+ and neutral H densities, similar to Zirnstein et al. (2020b). We scale our interstellar H^+ density everywhere outside the heliopause by a factor 0.6, thus maintaining the total dynamic pressure of the simulation but correcting for the relative abundance of interstellar He^+. We also scale the interstellar neutral H density by the same fraction, as a first-order estimation, in order to account for the proper filtration of interstellar neutral H by charge exchange through the SW-VLISM interaction. Effectively, the pristine interstellar neutral H density decreases from $0.154\,cm^{-3}$ to $0.092\,cm^{-3}$. This value is very similar to the neutral H density expected near the upwind TS location derived from spacecraft observations near 1 au (Bzowski et al. 2009), implying a particularly high filtration factor (ratio of neutral H density at the TS to the pristine VLISM) of ~1. We note that this scaling is only an approximation, and that a more self-consistent simulation is required to determine the nonlinear effects of He on the SW-VLISM interaction. For the purposes of our study, however, a simple scaling of the interstellar H^+/H densities can inform us of how the geometry of the ribbon may be affected. We also note that our approach of scaling the MHD/kinetic simulation's plasma and neutral densities in the OHS by a factor of 0.6 during charge exchange to mimic the presence of interstellar He^+ is different than if we were to increase the plasma mass density to add He^+, which effectively increases the dynamic pressure of the interstellar plasma. For example, Izmodenov et al. (2003) showed that adding interstellar He^+ on top of an existing interstellar H^+ density increases the dynamic pressure of the interstellar plasma and pushes the heliopause boundary inward toward the Sun. In contrast, we assume that our MHD simulation's plasma density already contains the $H^+ + He^+$ mixture, and the plasma dynamic pressure is consistent with the mixture since our heliopause boundary is already consistent with Voyager observations. Therefore, we do not need to change the simulation properties except during charge exchange since the MHD plasma density is no longer assumed to be just H^+, but a mixture of H^+ and He^+. Thus, we must decrease the interstellar H and H^+ densities during charge exchange in our ribbon model calculations.

Figure 7 shows the simulated ribbon center maps for each model with and without the presence of interstellar He. It is worth noting first that the fluxes for each model change differently in the presence of interstellar He. The decrease of the weak-scattering model fluxes is straightforward to understand, as it is a direct consequence of a 40% decrease in charge-exchange rate, and thus secondary ENA production rate, outside the heliopause. As in our previous work (Zirnstein et al. 2020b), decreasing the interstellar H^+ and neutral H densities decreases the weak-scattering ribbon fluxes by a similar fraction.

In the strong-scattering model, however, we note a few potential consequences from changing the interstellar densities. First, the rate of ions streaming into the retention region, and thus an enhancement in ENA-producing ions, depends on the Alfvén wave speed. Through careful consideration, however, our simulated Alfvén speed actually does not change between the models with and without the presence of interstellar He. The reason for this is because our MHD simulation assumes the interstellar proton density, n_p, is the total effective interstellar plasma density, such that $n_p m_{H+} = n_{H+} m_{H+} + n_{He+} m_{He+}$. Thus, even though we did not include the presence of interstellar He in the first case, it does account for the total effective plasma density. Therefore, the Alfvén speed remains the same in both cases. Second, it is immediately clear from Figure 7 that the strong-scattering model fluxes do not decrease as significantly as the weak-scattering model fluxes. We determine that this is due to the decrease in interstellar neutral H density. Examining Equation (A27) in Schwadron & McComas (2013), the amplitude of the PINS distribution inside the retention region depends on the rate of neutralization (or loss) of PINS by charge exchange. With a decreased interstellar neutral H density, the charge-exchange timescale τ_x increases by the same factor. Since $\tau_x v_A \gg \tau_1 v/2$ in our simulation, the distribution of ions close to $\boldsymbol{B}\cdot\boldsymbol{r} = 0$ increases nearly proportionally to τ_x, almost compensating for the decrease in ribbon ENA production. Far from the retention region, however, ions are not being scattered by Alfvén waves and thus only the ribbon ENA production rate is affected. This, effectively, increases the distribution of ions nearer to $\boldsymbol{B}\cdot\boldsymbol{r} = 0$ and thus increases the secondary ENA flux, almost compensating for the lower ENA production rate.

Figures 8 and 9 compare the mean centers and radii of the simulated ribbon with and without the presence of interstellar He for each model. It is clear that the presence of interstellar He changes the ribbon's center differently for each model. The center of the weak-scattering ribbon model moves slightly closer along the *B*–*V* plane toward the pristine ISMF direction ($\boldsymbol{B}_{OB}$). This is simply due to the fact that a decrease in interstellar proton density increases the neutral SW mean free path in the OHS, creating more ENAs farther from the heliosphere in the less-draped ISMF. Directions in the sky that satisfy $\boldsymbol{B}\cdot\boldsymbol{r} = 0$ are now less affected by field line draping around the heliosphere and more closely approximates a great circle in the sky with a center closer to $\boldsymbol{B}_{OB}$. The ribbon radii for the weak-scattering model (Figure 9, right panel) increase by a few degrees for the same reason: the source of ribbon ENAs are now farther from the heliosphere in a less-draped ISMF, such that directions in the sky satisfying $\boldsymbol{B}\cdot\boldsymbol{r} = 0$ are closer to a circle with larger angular radius.

Interestingly, the strong-scattering model ribbon behaves quite differently. The ribbon center does not change as significantly compared to the weak-scattering model, and even moves slightly farther away from $\boldsymbol{B}_{OB}$. Since the uncertainties of the ribbon centers in both cases nearly overlap, this change may be statistically insignificant. The ribbon radii for the strong-scattering model also do not change significantly, where the centers overlap at all energies. The reasons for this lack of change is likely related to how the strong-scattering (or spatial retention) model works. The rate of ion retention is higher in the draped and compressed ISMF close to the heliopause, as described by Zirnstein et al. (2019a), producing a higher ribbon ENA production closer to the heliopause. Therefore, even if the interstellar H^+ density decreases everywhere by the same fraction, more ions are retained in the retention region close to the heliopause than farther away. Interestingly, this is not significantly affected by a change in interstellar H^+ density.

It is not yet clear how the inclusion of interstellar He+ and neutral He will dynamically affect the SW-VLISM interaction in our simulation, especially when $He + He^+$ charge exchange is included. If the bow wave/shock interaction is strongly affected (e.g., McComas et al. 2012; Scherer & Fichtner 2014),

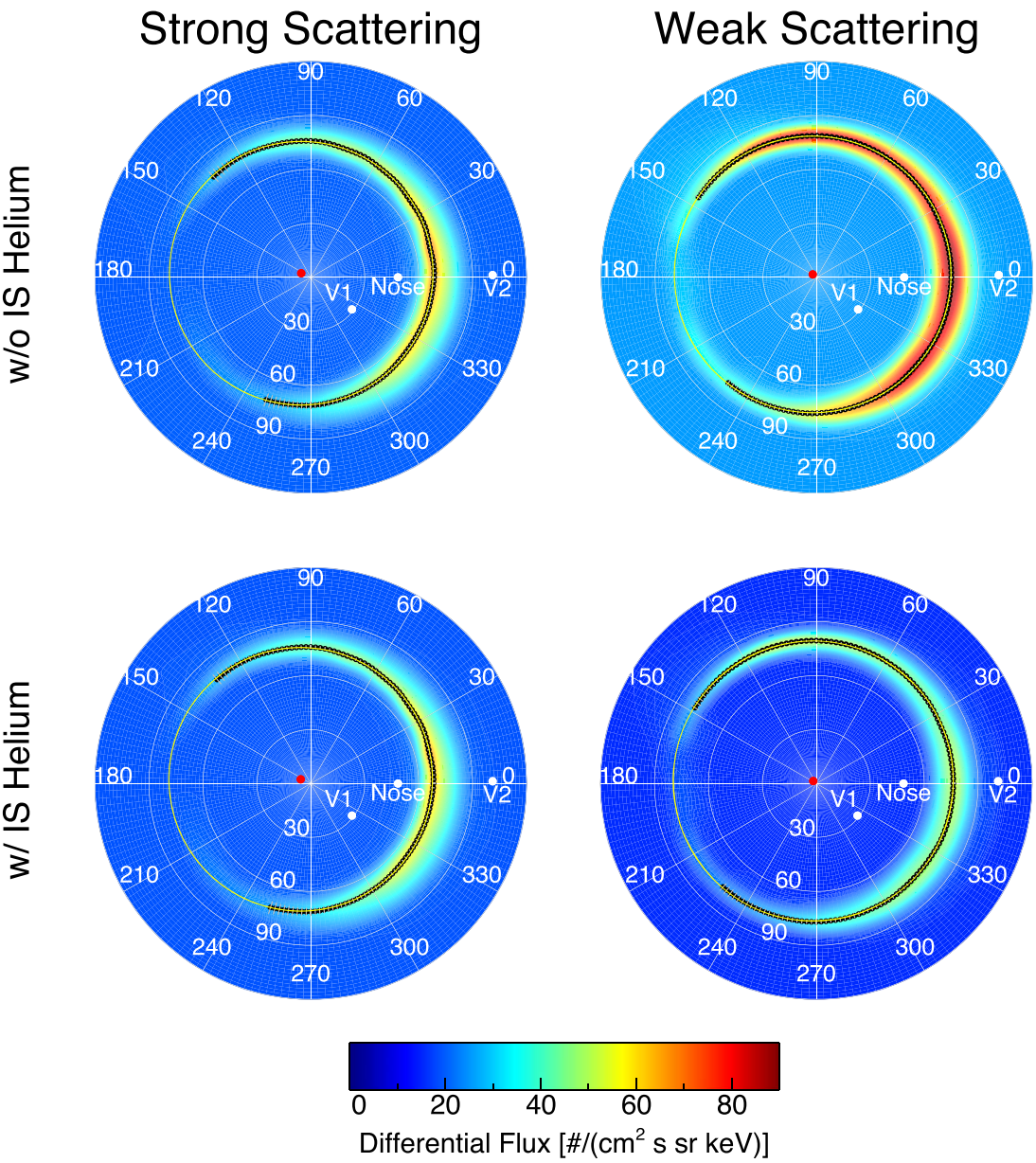

Figure 7. Simulated ribbon-centered maps at 1.1 keV for each ribbon model (columns), with and without the presence of interstellar He (rows). The locations of the peak ribbon flux, circle fits to the peak locations, and the derived ribbon centers are also shown, similar to Figure 1. Note that the color bar range is the same for all panels.

which in turn could affect the draping structure of the ISMF around the heliosphere, then it is possible that the geometry of the ribbon could be affected. We note, however, that our current MHD simulation includes the total effective plasma density, and thus the Alfvén wave speed in the VLISM, would not significantly change when interstellar He is included. On the other hand, a smaller interstellar H^+ density allows more neutralized SW/PUI atoms to propagate away from the heliopause and upstream of the bow shock/wave, effectively modifying the shock's upstream boundary conditions and making it less likely to be a shock (see also Zank et al. 2013). This will be the subject of a future study.

4. Discussion and Conclusions

It is generally believed that the IBEX ribbon is produced by the propagation of secondary ENAs from outside the heliopause. However, the physical processes controlling the parent PINS distribution are not well understood. In particular, it is not clear whether the pitch-angle scattering of PINS is sufficiently rapid as to nearly isotropize the PINS distribution before charge exchange occurs, or that PINS are able to maintain largely anisotropic pitch-angle distributions before experiencing charge exchange.

4.1. Discussion of the Ribbon Geometry

The goal of our study is to show how the two limits of pitch-angle scattering, strong scattering via the spatial retention method proposed by Schwadron & McComas (2013) and the limit of negligible scattering, affect the geometry of the ribbon. We simulated the ribbon under these two pitch-angle-scattering limits including the angular and energy response functions of the IBEX-Hi instrument and quantify the geometry (center and

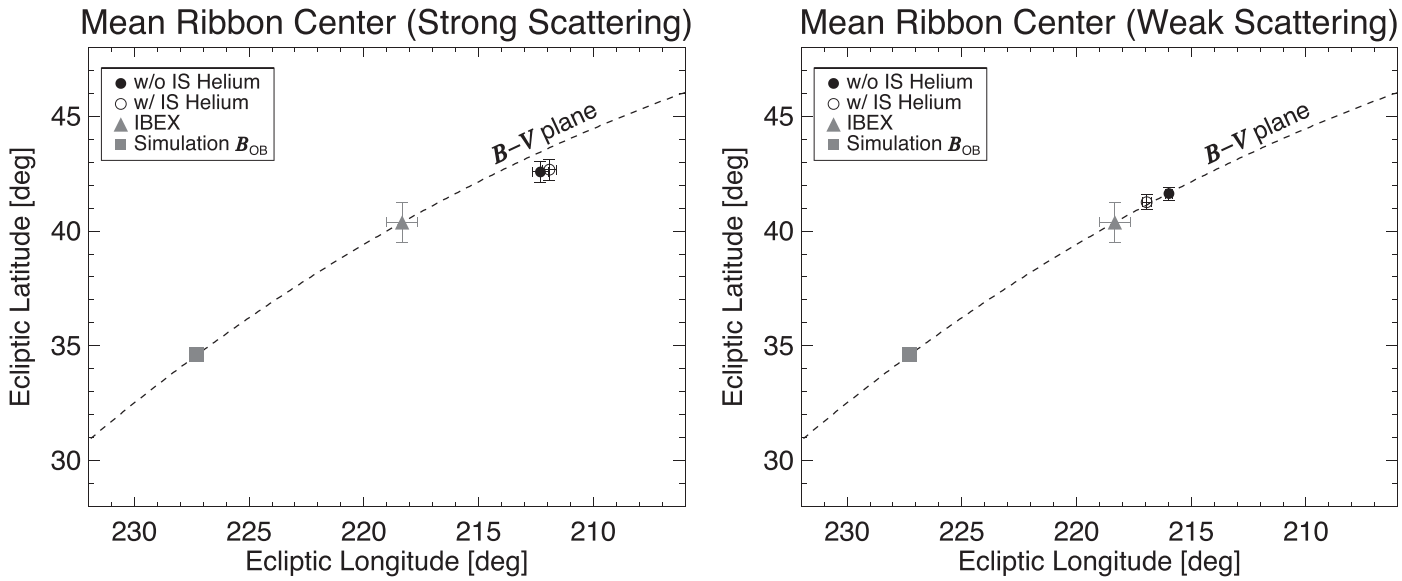

Figure 8. Comparison of the simulated mean ribbon centers with and without the presence of interstellar He for both ribbon models. The mean ribbon centers are weight averaged over energy.

radius) of the ribbon as a function of ENA energy. The main results of our study can be summarized as follows:

1. The simulated ribbon centers are spread out in ecliptic latitude as a function of ENA energy for both pitch-angle scattering limits, qualitatively similar to IBEX observations, but to a lower degree. The spread is slightly greater for the strong-scattering limit, and the mean locations of the ribbon center (weighted over energy) are $\sim 2^\circ$ and $\sim 5^\circ$ away from the IBEX ribbon center for the weak and strong-scattering limits, respectively. However, the mean ribbon centers both lie close to the *B*–*V* plane of the heliosphere.
2. The simulated ribbon radii in the weak-scattering limit are $\sim 4^\circ$ larger than IBEX observations at 1.1, 1.7, and 2.7 keV, which are the most reliable simulated ENA energies. The simulated ribbon radii in the strong-scattering limit are statistically consistent with IBEX observations at these energies.
3. The consistency of the ribbon radii in the strong-scattering limit suggests the magnitude of the pristine ISMF in our simulation, 2.93 μG, is consistent with observations. However, in order to correct for the larger ribbon radii in the weak-scattering limit, the pristine ISMF magnitude would need to decrease by ~ 1.25 μG. However, numerous studies of the pristine ISMF suggest that a magnitude of $\lesssim 2$ μG is unrealistically low. This suggests that the strong-scattering limit is more likely responsible for the ribbon's origin, at least in terms of the ribbon's geometry. Both of our ribbon models, however, appear to underestimate the observed ribbon flux in the presence of interstellar He, and both underestimate the angular spread in ribbon center as a function of energy.
4. The angular offset of the mean simulated ribbon centers from the observations suggest that, if one of the scattering limits is true, the direction of the pristine ISMF far from the heliosphere ($\boldsymbol{B}_{\rm OB}$ in our simulation) is slightly offset from our simulated value. The pristine ISMF would need to be shifted along the *B*–*V* plane toward the VLISM inflow direction by $\sim 2^\circ$ or $\sim 5^\circ$ for the weak and strong-scattering limits in order for their ribbon centers to be more consistent with IBEX observations.
5. When we heuristically include the presence of interstellar He in our models of the ribbon, we find that the total flux of the ribbon decreases by $\sim$40% in the weak-scattering case due to a similar drop in the charge-exchange rate. However, the ribbon flux remains approximately the same in the strong-scattering case due to an increase in the PINS distribution near $\boldsymbol{B} \cdot \boldsymbol{r} = 0$.
6. The presence of interstellar He decreases the angular distance between the IBEX ribbon center and the ribbon simulated in the weak-scattering limit by $\sim 1^\circ$. Conversely, the ribbon radii in the weak-scattering limit increase by $\sim 2^\circ$. These behaviors are consistent with the fact that the mean free path of neutralized SW atoms propagating through the VLISM is larger, generating PINS farther from the heliopause in the less-draped ISMF. This produces ribbon fluxes closer to a great circle in the sky (larger ribbon radii) with a center closer to $\boldsymbol{B}_{\rm OB}$.
7. The presence of interstellar He slightly increases the angular distance between the IBEX ribbon center and the ribbon simulated in the strong-scattering limit (increases $\sim 0.^\circ 3$). The simulated ribbon radii do not change. This behavior suggests that, unlike the weak-scattering limit, the PINS distribution in the strong-scattering limit is still enhanced near $\boldsymbol{B} \cdot \boldsymbol{r} = 0$ close to the heliopause. While the neutralized SW atoms can travel farther from the heliopause, a decrease in interstellar neutral H atoms increases the PINS distribution close to the heliopause, approximately compensating for the change in interstellar densities.

The results of our study show that the geometry of the ribbon is moderately sensitive to the physical mechanisms controlling the parent PINS distribution in the VLISM. While we are not yet able to definitively determine whether the ribbon in strong- or weak-scattering limits is more realistic, we find that, in order for these different models to reproduce IBEX observations, the pristine ISMF far from the heliosphere may be slightly different from our previous analysis (Zirnstein et al. 2016b) by a few degrees. It

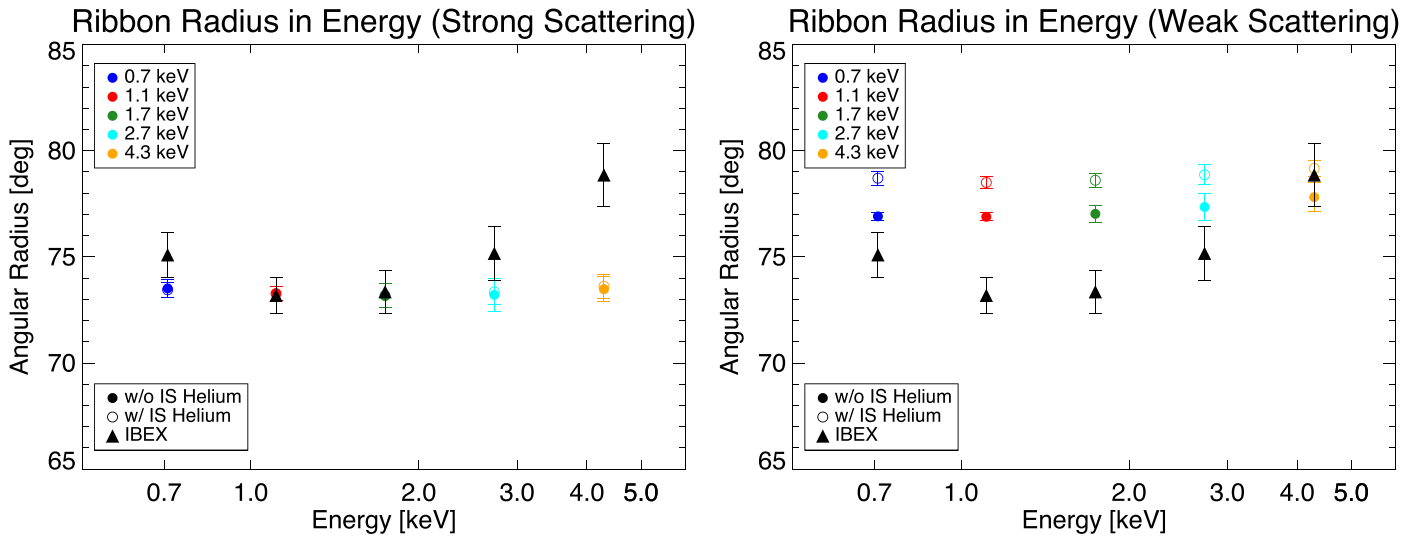

Figure 9. Comparison of the simulated ribbon radii with and without the presence of interstellar (IS) He for both ribbon models.

seems unlikely that the ribbon is formed primarily under weak pitch-angle scattering, since our results suggest this would require an unrealistically smaller magnitude of the pristine ISMF far from the heliosphere. The strong-scattering limit seems more likely as it better reproduces the observed ribbon radius at ∼1.1–2.7 keV, if the pristine ISMF is shifted by ∼5° along the *B*–*V* plane toward the VLISM inflow direction.

Finally, we note that our simulated ribbon geometry results are not very sensitive to our choice of interstellar H density. We have tested our choice of the neutral SW distribution in Section 2.2, Equation (1), by changing the neutral H density to a constant value of 0.09 cm^{-3} between the Sun and TS, rather than as a function of distance due to filtration by charge exchange, and derive similar results for the ribbon geometry as those shown in Table 1.

4.2. Discussion of the Ribbon Intensity

We note, however, that the simulated ribbon intensities underestimate the observations, especially in the strong-scattering case. Moreover, neither the weak-scattering nor the strong-scattering models we employ in this study are able to reproduce the large spread in ribbon center as a function of energy, contrary to Swaczyna et al. (2016). The reason for this may be due to the fact that Swaczyna et al. (2016) did not model the ribbon with a draped ISMF, where directions in the sky that satisfy $\boldsymbol{B} \cdot \boldsymbol{r} = 0$ change as a function of distance from the heliopause.

Interestingly, by estimating the effects of interstellar He on our results, the simulated ribbon intensities are similar in the weak- and strong-scattering cases and both significantly underestimate the observed ribbon fluxes. We can offer three possible reasons for this discrepancy.

1. Zirnstein et al. (2020b) simulated the evolution of the IBEX ribbon in the presence of the evolving SW and interstellar shocks, and were able to approximately reproduce the observed ribbon evolution and overall intensity under the assumption of the weak-scattering limit and in the presence of interstellar He (in a manner similar to the current study). It is possible that a time-dependent model of the ribbon is necessary to properly reproduce the observed IBEX ribbon intensity, which is not the same as the time-averaged neutral SW model employed in the current study.
2. Zirnstein et al. (2020a) simulated a scenario of the ribbon in the presence of interstellar turbulence consistent with Voyager 1 observations. Effectively, their model is similar to the weak-scattering limit except that the parent PINS can scatter in pitch angle near $\boldsymbol{B} \cdot \boldsymbol{r} = 0$ and be trapped in a magnetic bottle. The scattering is minor compared to the "strong" scattering scenario from Schwadron & McComas (2013), which achieves nearly isotropic distributions, but slightly enhances the number of ENAs generated from directions near $\boldsymbol{B} \cdot \boldsymbol{r} = 0$ compared to the "weak" (or zero) scattering scenario as presented in the current study. This, effectively, increases the ribbon flux compared to the weak-scattering scenario without any turbulent scattering.
3. Swaczyna et al. (2020) show that the interstellar neutral H density is likely ∼40% higher than previously thought, based on New Horizons' SWAP observations of interstellar PUIs. We expect that a higher neutral H density would increase our simulated ribbon flux by a factor of ∼1.4, partially compensating for our models' low ribbon fluxes.

E.Z., M.D., and J.H. acknowledge support from NASA grant 80NSSC17K0597. E.Z. and J.H. also acknowledge support from NASA grant 80NSSC18K1212. E.Z. thanks Pawel Swaczyna for helpful discussions. The work reported in this paper was partly performed at the TIGRESS high-performance computer center at Princeton University which is jointly supported by the Princeton Institute for Computational Science and Engineering and the Princeton University Office of Information Technology's Research Computing department.

ORCID iDs

E. J. Zirnstein https://orcid.org/0000-0001-7240-0618
M. A. Dayeh https://orcid.org/0000-0001-9323-1200
J. Heerikhuisen https://orcid.org/0000-0001-7867-3633

References

Bzowski, M., Czechowski, A., Frisch, P. C., et al. 2019, ApJ, 882, 60
Bzowski, M., & Heerikhuisen, J. 2020, ApJ, 888, 24
Bzowski, M., Möbius, E., Tarnopolski, S., Izmodenov, V., & Gloeckler, G. 2009, SSRv, 143, 177
Chalov, S. V., Alexashov, D. B., McComas, D., et al. 2010, ApJL, 716, L99
Dayeh, M. A., Zirnstein, E. J., Desai, M. I., et al. 2019, ApJ, 879, 84

Florinski, V., & Heerikhuisen, J. 2017, ApJ, 838, 50
Florinski, V., Heerikhuisen, J., Niemiec, J., & Ernst, A. 2016, ApJ, 826, 197
Funsten, H. O., Allegrini, F., Bochsler, P., et al. 2009a, SSRv, 146, 75
Funsten, H. O., Allegrini, F., Crew, G. B., et al. 2009b, Sci, 326, 964
Funsten, H. O., DeMajistre, R., Frisch, P. C., et al. 2013, ApJ, 776, 30
Gamayunov, K., Zhang, M., & Rassoul, H. 2010, ApJ, 725, 2251
Grygorczuk, J., Ratkiewicz, R., Strumik, M., & Grzedzielski, S. 2011, ApJL, 727, L48
Gurnett, D. A., Kurth, W. S., Burlaga, L. F., & Ness, N. F. 2013, Sci, 341, 1489
Heerikhuisen, J., & Pogorelov, N. V. 2011, ApJ, 738, 29
Heerikhuisen, J., Pogorelov, N. V., Florinski, V., Zank, G. P., & Kharchenko, V. 2009, in ASP Conf. Ser. 406, Numerical Modeling of Space Plasma Flows: ASTRONUM-2008, ed. N. V. Pogorelov et al. (San Francisco, CA: ASP), 189
Heerikhuisen, J., Pogorelov, N. V., Zank, G. P., et al. 2010, ApJL, 708, L126
Heerikhuisen, J., Zirnstein, E. J., Funsten, H. O., Pogorelov, N. V., & Zank, G. P. 2014, ApJ, 784, 73
Izmodenov, V., Malama, Y. G., Gloeckler, G., & Geiss, J. 2003, ApJL, 594, L59
Izmodenov, V. V., & Alexashov, D. B. 2015, ApJS, 220, 32
Izmodenov, V. V., & Alexashov, D. B. 2020, A&A, 633, L12
Izmodenov, V. V., Malama, Y., & Ruderman, M. S. 2005, A&A, 429, 1069
Kubiak, M. A., Bzowski, M., Sokół, J. M., et al. 2014, ApJS, 213, 29
Lindsay, B. G., & Stebbings, R. F. 2005, JGR, 110, A12213
Markwardt, C. B. 2009, in ASP Conf. Ser. 411, Astronomical Data Analysis Software and Systems XVIII, ed. D. A. Bohlender, D. Durand, & P. Dowler (San Francisco, CA: ASP), 251
McComas, D. J., Alexashov, D., Bzowski, M., et al. 2012, Sci, 336, 1291
McComas, D. J., Allegrini, F., Bagenal, F., et al. 2008a, SSRv, 140, 261
McComas, D. J., Allegrini, F., Bochsler, P., et al. 2009a, SSRv, 146, 11
McComas, D. J., Allegrini, F., Bochsler, P., et al. 2009b, Sci, 326, 959
McComas, D. J., Bzowski, M., Fuselier, S. A., et al. 2015, ApJS, 220, 22
McComas, D. J., Dayeh, M. A., Funsten, H. O., et al. 2018b, ApJL, 856, L10
McComas, D. J., Ebert, R. W., Elliott, H. A., et al. 2008b, GeoRL, 35, L18103
McComas, D. J., Zirnstein, E. J., Bzowski, M., et al. 2017, ApJS, 229, 41
Möbius, E., Bochsler, P., Bzowski, M., et al. 2009, Sci, 326, 969
Müller, H.-R., & Zank, G. P. 2004, in AIP Conf. Proc. 719, Physics of the Outer Heliosphere, ed. V. Florinski, N. V. Pogorelov, & G. P. Zank (Melville, NY: AIP), 99
Opher, M., Alouani Bibi, F., Toth, G., et al. 2009, Natur, 462, 1036
Parker, E. N. 1961, ApJ, 134, 20
Pogorelov, N. V., Fichtner, H., Czechowski, A., et al. 2017a, SSRv, 212, 193
Pogorelov, N. V., Heerikhuisen, J., Roytershteyn, V., et al. 2017b, ApJ, 845, 9
Pogorelov, N. V., Stone, E. C., Florinski, V., & Zank, G. P. 2007, ApJ, 668, 611
Pogorelov, N. V., Suess, S. T., Borovikov, S. N., et al. 2013, ApJ, 772, 2
Pogorelov, N. V., Zank, G. P., Borovikov, S. N., et al. 2008, in ASP Conf. Ser. 385, Numerical Modeling of Space Plasma Flows, ed. N. V. Pogorelov, E. Audit, & G. P. Zank (San Francisco, CA: ASP), 180
Press, W. H., Teukolsky, S. A., Vetterling, W. T., & Flannery, B. P. 2007, Numerical Recipes in C++: The Art of Scientific Computing (3rd ed.; Cambridge: Univ. Press Cambridge)
Ratkiewicz, R., & Grygorczuk, J. 2008, GeoRL, 35, L23105
Ratkiewicz, R., Strumik, M., & Grygorczuk, J. 2012, ApJ, 756, 3
Reisenfeld, D. B., Bzowski, M., Funsten, H. O., et al. 2019, ApJ, 879, 1
Scherer, K., & Fichtner, H. 2014, ApJ, 782, 25
Schlickeiser, R. 1989, ApJ, 336, 243
Schwadron, N. A., Adams, F. C., Christian, E. R., et al. 2014a, Sci, 343, 988
Schwadron, N. A., Allegrini, F., Bzowski, M., et al. 2011, ApJ, 731, 56
Schwadron, N. A., Allegrini, F., Bzowski, M., et al. 2018, ApJS, 239, 1
Schwadron, N. A., & McComas, D. J. 2013, ApJ, 764, 92
Schwadron, N. A., & McComas, D. J. 2019, ApJ, 887, 247
Schwadron, N. A., Moebius, E., Fuselier, S. A., et al. 2014b, ApJS, 215, 13
Sokół, J. M., McComas, D. J., Bzowski, M., & Tokumaru, M. 2020, ApJ, 897, 179
Sokół, J. M., Swaczyna, P., Bzowski, M., & Tokumaru, M. 2015, SoPh, 290, 2589
Stone, E. C., Cummings, A. C., Heikkila, B. C., & Lal, N. 2019, NatAs, 3, 1013
Stone, E. C., Cummings, A. C., McDonald, F. B., et al. 2013, Sci, 341, 150
Swaczyna, P., Bzowski, M., & Sokół, J. M. 2016, ApJ, 827, 71
Swaczyna, P., McComas, D. J., Zirnstein, E. J., et al. 2020, ApJ, 903, 48
Swaczyna, P., McComas, D. J., Zirnstein, E. J., & Heerikhuisen, J. 2019, ApJ, 887, 223
Zank, G. P. 1999, SSRv, 89, 413
Zank, G. P. 2015, ARA&A, 53, 449
Zank, G. P., Heerikhuisen, J., Wood, B. E., et al. 2013, ApJ, 763, 20
Zhang, M., Pogorelov, N. V., Zhang, Y., Hu, H. B., & Schlickeiser, R. 2020, ApJ, 889, 97
Zirnstein, E. J., Funsten, H. O., Heerikhuisen, J., & McComas, D. J. 2016a, A&A, 586, A31
Zirnstein, E. J., Giacalone, J., Kumar, R., et al. 2020a, ApJ, 888, 29
Zirnstein, E. J., Heerikhuisen, J., & Dayeh, M. A. 2018a, ApJ, 855, 30
Zirnstein, E. J., Heerikhuisen, J., Funsten, H. O., et al. 2016b, ApJL, 818, L18
Zirnstein, E. J., Heerikhuisen, J., & McComas, D. J. 2015a, ApJL, 804, L22
Zirnstein, E. J., Heerikhuisen, J., McComas, D. J., et al. 2018b, ApJ, 859, 104
Zirnstein, E. J., Heerikhuisen, J., Pogorelov, N. V., McComas, D. J., & Dayeh, M. A. 2015b, ApJ, 804, 5
Zirnstein, E. J., Heerikhuisen, J., Zank, G. P., et al. 2017, ApJ, 836, 238
Zirnstein, E. J., Kim, T. K., Mostafavi, P., et al. 2020b, ApJ, 891, 56
Zirnstein, E. J., McComas, D. J., Schwadron, N. A., et al. 2019a, ApJ, 876, 92
Zirnstein, E. J., Swaczyna, P., McComas, D. J., & Heerikhuisen, J. 2019b, ApJ, 879, 106